Hydrography and high-temperature heat flux of the Rainbow hydrothermal site (36°14′N, Mid-Atlantic Ridge)

A. M. Thurnherr
Department of Oceanography, Florida State University, Tallahassee, Florida

K. J. Richards
School of Ocean and Earth Science, Southampton Oceanography Centre, Southampton, England, United Kingdom

Abstract

On the basis of an extensive set of conductivity-temperature-depth, lowered acoustic Doppler current profiler (LADCP), and nephelometry profiles and tow-yos the hydrography, flow field, and particle plume of the Rainbow hydrothermal site on the Mid-Atlantic Ridge are analyzed. In the rift valley the water column is less dense and stratified than both eastern and western off-ridge water, with T/S characteristics consistent with inflow across a sill from the east. The buoyant hydrothermal plumes rise into a strong boundary current flowing along the slope of a topographic high which partially blocks the rift valley below $1950\,\mathrm{m}$. The bulk of the neutrally buoyant plume is advected across a sill which forms both the narrowest and the shallowest part of the valley and acts as a hydraulic control point for the flow below $2000\,\mathrm{m}$. Large-amplitude internal waves consistent with tidal forcing are observed near the sill, but LADCP measurements suggest that the tidal signal is not strong enough to lead to flow reversal at plume depth. Above $2000\,\mathrm{m}$ the mean current across the topography generates lee waves which radiate energy upward and downstream. Density-averaged light-scattering profiles show the hydrothermal particle plume to be Gaussian in depth, even in the near field, where many of the individual profiles are characterized by multiple peaks and the horizontal variability is highest. The temperature anomalies associated with the mean near-source particle plume are of order $-5 \times 10^{-3}\ ^\circ\mathrm{C}$; that is, the plume is cold/fresh as expected from the background hydrography of the deep Atlantic. Using the flow field, light-scattering, and hydrographic anomaly observations, the heat flux associated with the hydrothermal particle plume at Rainbow is estimated to lie between 1 and $5\,\mathrm{GW}$.

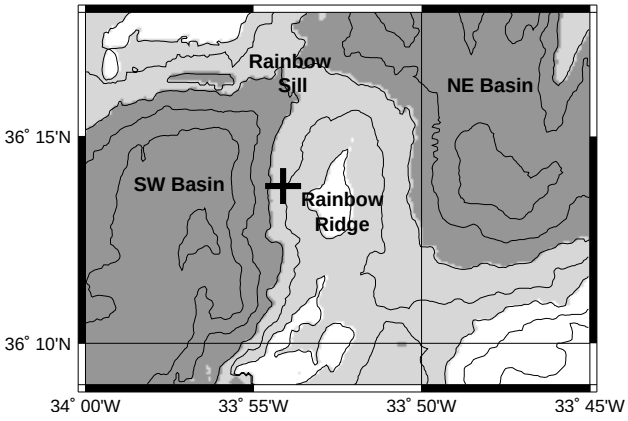

Figure 1. Rainbow region bathymetry and nomenclature. Darkly shaded regions are deeper than $2500\,\mathrm{m}$, lightly shaded regions are between 2000 and $2500\,\mathrm{m}$, and unshaded regions are $<2000\,\mathrm{m}$ deep; contour interval is $250\,\mathrm{m}$. The black cross near the $2250\,\mathrm{m}$ contour marks the location of the hydrothermal vent field. The SW and NE basins are part of the MAR rift valley; the unshaded regions in the SE and NW corners form part of the valley walls.

1. Introduction

Hydrothermal processes account for approximately one third of the global geothermal heat flux to the oceans and strongly affect their chemical composition. For some chemical species, hydrothermal input constitutes a source of similar magnitude to riverine input, while particle precipitation in hydrothermal plumes removes others [see *Elderfield and Schultz,* 1996]. The most spectacular manifestations of hydrothermal circulation are the high-temperature ($\approx 350^\circ\mathrm{C}$) vent fields which give rise to particle-rich plumes rising hundreds of meters above the seafloor, where they spread laterally into the surrounding water column. These focused inputs of heat and chemicals support distinct and fascinating ecosystems [e.g., *Tunnicliffe,* 1991]. Even though high-temperature fluxes may not amount to more than a fraction of the hydrothermal total [e.g., *Schultz and Elderfield,* 1997], they are still significant in terms of dispersal of larvæ and chemicals by the equilibrium plumes (neutrally buoyant without vertical momentum). Furthermore, they provide constraints for the physical and chemical processes in hydrothermal circulation.

There are several different approaches for estimating the high-temperature fluxes from a hydrothermal site, including direct measurements at the vent orifices to yield instantaneous fluxes from the individual sources [e.g., *Ginster et al.,* 1994] and measurements in the equilibrium plumes to derive an integrated view of the source conditions, possibly including some of the low-temperature ("diffuse") fluxes close to the vents. A number of different techniques have been used to estimate integrated fluxes from equilibrium plumes, including height-of-rise modeling [e.g., *Rudnicki and Elderfield,* 1992], advection of hydrographic anomalies [e.g., *Baker and Massoth,* 1987], and plume age estimates based on chemical anomaly ratios [e.g., *Rosenberg et al.,* 1988].

To be able to interpret chemical and physical plume observations, a good understanding of the local hydrography and flow regime is paramount. Without detailed knowledge of the background hydrography it is not possible to determine which temperature/salinity signals are caused by the hydrothermal activity. Without a conceptual model of the background flow regime, which determines the trajectory of the spreading plumes, interpretation of chemical and physical anomalies remains tenuous at best. The hydrography and flow field are strongly interlinked and must be analyzed together.

The goal of this work is to present the results of the first detailed study of the spatial and temporal variability of the hydrography, flow regime, and particle plume observations within a segment of the Mid-Atlantic Ridge (MAR) rift valley in the immediate vicinity of a hydrothermal vent field, and to apply these results to estimate the heat flux associated with the hydrothermal particle plume.

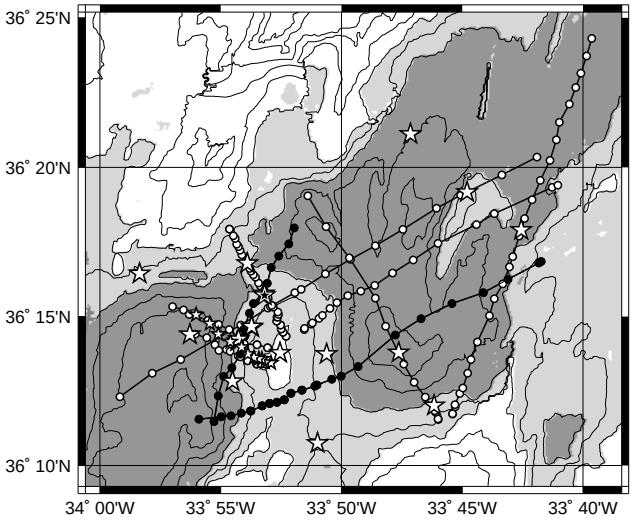

Figure 2. FLAME stations. Bathymetric shading and contours are the same as in Figure 1; CTD stations are marked with stars and BRIDGET tow-yos are marked with open and solid circles; small open stars on the western slope of Rainbow Ridge indicate the track of a CTD tow-yo. The BRIDGET tows marked with solid circles are the cross-sill tow of Figure 10 and the cross-ridge tow of Figure 11. The solid star with a white border near Rainbow Sill indicates the position of the CTD yo-yo of Figure 12.

1.1. Rainbow Hydrothermal Site

The Rainbow site (Figure 1) was discovered in the course of a large-scale survey of the MAR [*German et al.*, 1996b]. On the basis of water column light-transmission anomalies, it was chosen for a preliminary study using seven conductivity-temperature-depth (CTD) casts [*German et al.*, 1996a] and for testing the British Mid-Ocean Ridge Initiative hydrothermal deep-tow instrument (BRIDGET), which was used to map the hydrothermal particle plume over a horizontal extent of 10–15 km [*Rudnicki et al.*, 1995]. During May and June 1997 a detailed study, the Fluxes at Amar Experiment (FLAME), was undertaken to investigate the hydrography, plume dynamics, chemistry, and biology of the Rainbow site, the preliminary findings of which were reported by *German et al.* [1998]. On the basis of the FLAME data, the spreading equilibrium plume can be traced for several tens of kilometers. During a subsequent submersible dive the active hydrothermal vents were discovered between 2270 and 2320 m at 36°13.80′N, 33°54.12′W [*Fouquet et al.*, 1998].

Atlantic hydrothermal plumes differ from their Pacific counterparts in a number of important aspects, the most obvious of which is that Pacific plumes generally rise well above the surrounding topography before spreading under the influence of stratification and rotation, while the horizontal spreading of MAR plumes is usually confined by the rift valley walls. Apart from this direct influence the ridge topography also affects the plumes indirectly through the distinct hydrography of the MAR rift valley. *Saunders and Francis* [1985] show that the stratification of rift valley water is reduced in comparison to the abyssal waters found on either side of the ridge because of blocking by the valley walls, resulting in greater plume rise heights than would otherwise be the case.

In the Rainbow region the situation is further complicated by a topographic high which partially blocks the rift valley below 1950 m and separates it into a SW and a NE basin (Figure 1). Thus the topography is expected to largely determine the structure of the flow field and hydrography below that depth.

1.2. Methods

Two different instrument platforms were used to collect data at the stations shown in Figure 2: BRIDGET, developed for tow-yo lines through hydrothermal plumes [*Rudnicki et al.*, 1995] and a standard CTD package used primarily for vertical casts. In addition to the CTD stations shown, two eastern (≈50 km off axis) and one western (≈100 km off axis) background

stations were occupied for reference.

The BRIDGET platform was used to collect data between 1700 m (200 m above the highest particle plume observations; see section 4) and the seabed by tow-yoing it behind the ship at speeds not exceeding 1.5 knots. It was equipped with one and sometimes two self-contained FSI MicroCTD instruments, a Chelsea Instruments Aquatracka nephelometer (measuring light scattering at a 90° angle), as well as a 12-bottle sampling rosette and auxiliary instruments such as attitude sensors and an altimeter. The open and solid circles representing the BRIDGET tows in Figure 2 show the locations of the intersections of the tow-yo tracks with the 2100 m depth.

The CTD package was used for vertical profiles, a tow-yo, and a 10-hour yo-yo. It was equipped with a General Oceanics Neil Brown Mk3c CTD, a Chelsea Instruments Mk2 Subaquatracka nephelometer, a self-contained RDI Acoustic Doppler Current Profiler used as a lowered ADCP (LADCP), a 12-bottle sampling rosette, as well as auxiliary instruments such as an altimeter.

The temperature sensors of two of the three CTD instruments were precruise calibrated (the remaining one was taken as a spare). The Neil Brown CTD was recalibrated 10 months after the cruise. On the basis of the calibration information and direct instrument comparison on the BRIDGET platform the temperature intercalibration error is estimated to be $\pm 10^{-2}\,^{\circ}\mathrm{C}$. At 2100 m (the mean particle plume depth; see section 4) this corresponds to a density uncertainty of $\pm 2 \times 10^{-3}\,\mathrm{kg\,m^{-3}}$, the same order of magnitude as some of the important hydrographic patterns (e.g., see Figure 7). Therefore the hydrographic data sets from different instruments were not combined. Because the CTD data set is essentially a spatial subset of the BRIDGET data set (Figure 2), this is not a problem; the CTD data were used to verify the patterns observed in the BRIDGET data.

The conductivity sensor of the Neil Brown CTD was calibrated by analyzing 207 bottle samples with an Ocean Scientific International Autosal Model 8400A salinometer, resulting in an RMS error of 2.7×10^{-3} practical salinity units (psu). Because of hardware problems with one of the two CTD instruments flown on BRIDGET, not enough bottle samples were available to reliably calibrate the two conductivity sensors. The salinity calibration of one of the CTD instruments that failed twice during the cruise was judged to be too unreliable to be used at all. Therefore the measurements of this instrument were removed from the hydrographic data set. (The affected tows are not shown in Figure 2.) A trend of 5.8×10^{-4} psu per day was removed from the data of the second BRIDGET CTD instrument. The resulting T/S of the pressure-averaged data set was fitted against the corresponding Neil Brown T/S. To assess the quality of this intercalibration, the result was compared to the 37 available Autosal samples for the BRIDGET instrument resulting in an RMS error of 1.7×10^{-3} psu in the depth range 1600–2300 m. This corresponds to a density uncertainty of $\pm 1.5 \times 10^{-3}\,\mathrm{kg\,m^{-3}}$.

Nephelometry values ("nephels") are usually reported in arbitrary units [e.g., *Rudnicki and Elderfield,* 1992]; here instrument voltage (V) is used. To remove the offset between the CTD and the BRIDGET nephelometers as well as the trends observed during long BRIDGET tow-yos (caused by lens fogging), an offset was applied to the individual profiles by subtracting the mean value between 1500 m (or the upper turning point of the BRIDGET tow-yo profiles) and 1850 m (above the highest particle plume observations; see section 4). This results in some negative nephel values. To compare the response characteristics of the two nephelometers, the mean values (± 1 standard deviation) in the near-surface light-scattering maximum were calculated; the resulting agreement between $0.15\,(\pm 0.05)$ V, derived from 19 BRIDGET profiles, and $0.14\,(\pm 0.03)$ V, derived from 25 CTD profiles, indicates that the response characteristics of the two instruments are comparable.

The LADCP data presented here were derived from water track measurements calculated in 5-m bins. In contrast to the data presented by *German et al.* [1998], no averaging between the up- and the downcasts was performed. Average layer velocities were derived by separately calculating the mean of the northward and eastward velocity components; this method can produce small values in sheared layers where the velocity components take on both signs.

1.3. Outline

The regional hydrography of the Rainbow site is reviewed in section 2, followed by a description and interpretation of the rift valley hydrography and flow field (section 3). In section 4 the particle plume observations are presented. Combining the hydrographic, flow field and particle plume data, a heat flux estimate is derived in section 5. The results are discussed in section 6.

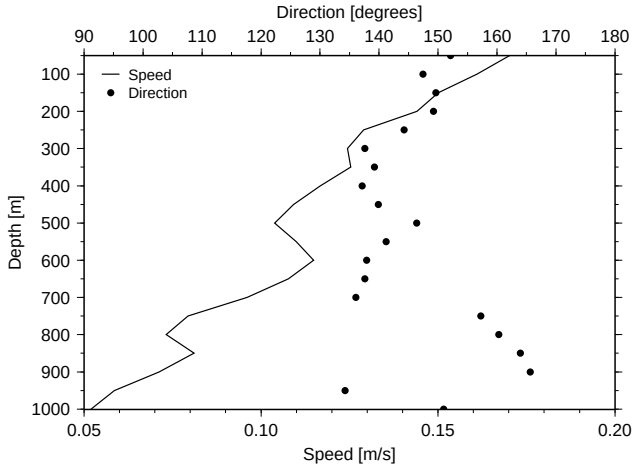

Figure 3. Mean LADCP-derived flow speed and direction in the top $1000\,\mathrm{m}$ of the water column. Each data point represents a $50\,\mathrm{m}$ vertical mean.

2. Regional Hydrography and Flow Field

The Rainbow site lies in a section of the MAR with a complex hydrography which is affected by the ridge topography, the Mediterranean water tongue, and the Azores Current and Front [e.g., *Wilson et al.*, 1995]. In the full-depth hydrographic profiles the Mediterranean water tongue is apparent as a layer of nearly constant salinity in the approximate θ_2 (potential temperature referenced to $2000\,\mathrm{dbar}$) range of $8°$–$10°\mathrm{C}$ (see Figure 4). The mean salinity maximum of $35.42\,\mathrm{psu}$ has an associated potential density σ_2 of $36.5\,\mathrm{kg\,m^{-3}}$ (σ_2 units will be omitted below). These values are consistent with published data [e.g., *Sy,* 1988]. The horizontal distribution of the Mediterranean outflow water can be traced as a wedge penetrating deep into the North Atlantic well beyond the MAR. According to *Sy* [1988] this wedge is bounded by two main branches of the Gulf Stream extension: the North Atlantic Current to the north ($\approx$46°N) and the Azores Current to the south. While the North Atlantic Current flows too far north to influence the Rainbow region, the latitude of the Azores Current near 34°W is not well defined. There is considerable evidence for meanders on a scale of at least $100\,\mathrm{km}$ [e.g., *Gould,* 1985; *Sy,* 1988].

Figure 3 shows the flow velocity in the top $1000\,\mathrm{m}$ of the water column, derived from the LADCP profiles of all CTD stations. The mean current flows mainly southeastward with the velocity decreasing nearly linearly from $0.17\,\mathrm{m\,s^{-1}}$ at the surface to $0.05\,\mathrm{m\,s^{-1}}$ at $1000\,\mathrm{m}$, below which the speed remains approximately constant down to the depth where the topography begins to influence the flow (see Figure 9). The magnitude and vertical structure of the observed current are consistent with geostrophic calculations presented by *Gould* [1985] and by *Sy* [1988], both reporting speeds around $0.25\,\mathrm{m\,s^{-1}}$ at the surface, decreasing nearly linearly to $0.05\,\mathrm{m\,s^{-1}}$ at $1000\,\mathrm{m}$ in the vicinity of the Rainbow site. *Gould* [1985] also proposes two criteria to assess if a given station lies north or south of the Azores Front: one for the depth of the $15°\mathrm{C}$ isotherm ($<300\,\mathrm{m}$ with typical values around $100\,\mathrm{m}$ north of the front) and the other for the surface salinity ($<36.4\,\mathrm{psu}$ with typical values near $36.2\,\mathrm{psu}$ north of the front). In the data presented here the respective mean values (±1 standard deviation) are $280 \pm 40\,\mathrm{m}$ and $36.3 \pm 0.2\,\mathrm{psu}$, indicating that the frontal region was sampled. The hydrography and current measurements of the FLAME cruise are therefore consistent with a southeastward flowing meander of the Azores Current influencing the top $1000\,\mathrm{m}$ of the water column.

Figure 4 shows the pressure-averaged θ_2/S diagrams of the CTD stations of the NE and SW basins as well as two off-ridge reference stations. The rift valley water characteristics are almost identical to those of the eastern off-ridge profile for $\sigma_2 > 36.7$ ($\approx$1300 m), while there is a significant difference between the rift valley and the western background station. Therefore the valley water most likely originates east of the MAR as was previously asserted by *German et al.* [1998]. The θ_2/S characteristics in the two basins separated by Rainbow Sill are virtually identical, indicating that the deep water of both basins most likely has the same origin. The potential temperature below $3000\,\mathrm{m}$ is similar in both basins ($3.64°$–$3.66°\mathrm{C}$). At $2600\,\mathrm{m}$ (the maximum depth of the deeper of the two eastern off-ridge background stations) the valley water is $\approx 0.6°\mathrm{C}$

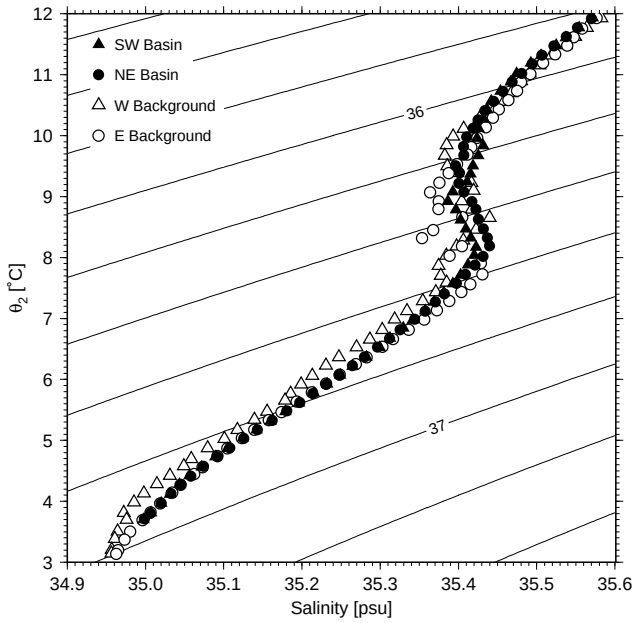

Figure 4. Mean water characteristics of the two deep basins on either side of Rainbow Ridge as well as the characteristics of an eastern and a western off-ridge background station. Potential-density contours are referenced to $2000\,\mathrm{dbar}$ (σ_2); contour interval is 0.2.

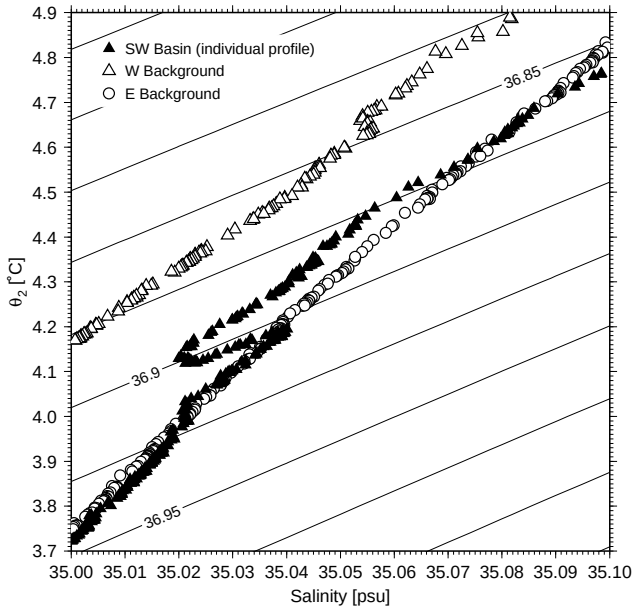

Figure 5. Interleaving of cold/fresh water between 1720 and 1920 m (σ_2 range 36.875–36.9) in a profile from the SW basin. Potential-density contours are referenced to $2000\,\mathrm{dbar}$ (σ_2); contour interval is 0.025.

warmer than eastern off-ridge water.

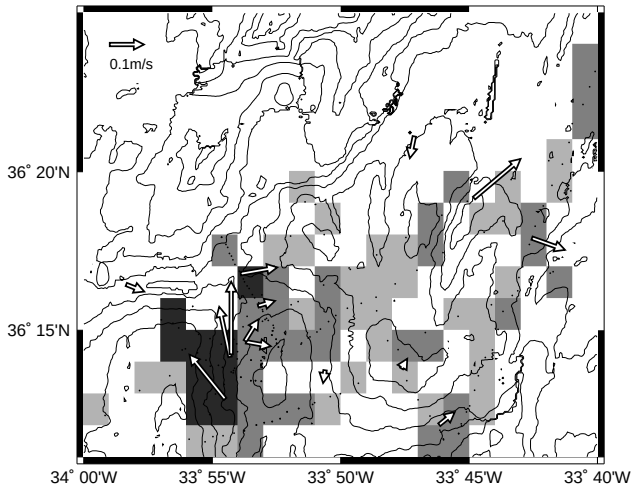

Figure 6. Mean horizontal density distribution (shaded cells) and instantaneous LADCP measurements (arrows) between 2175 and 2225 m. Bathymetric contours are the same as in Figure 1; lightly shaded cells indicate below-average potential densities, darkly shaded cells are more than 1 standard deviation ($\approx 3 \times 10^{-3}$) denser than the mean, and intermediately shaded cells lie in between.

Individual CTD profiles indicate that the situation in the rift valley is not as simple as the mean profiles suggest (Figure 5). Features such as the rift valley θ_2/S offset of approximately $-0.1°$C in the σ_2 range 36.875–36.9 are common in the SW basin. In the NE basin they are not observed away from the eastern slope of Rainbow Ridge (west of 33°50′W). These θ_2/S offsets do not coincide with the particle plume signatures (section 4) and are therefore assumed not to be caused by hydrothermal processes. (Detailed analysis of the hydrographic anomalies associated with the hydrothermal particle plume [*Thurnherr,* 2000] confirms this view.) Because there is no evidence for additional water masses in this region, the nonhydrothermal θ_2/S offsets are assumed to be caused by interleaving of western off-ridge water as inferred by *German et al.* [1998]. This is consistent with the approximate equality of the maximum depth of the interleaving structures (e.g., 1920 m in Figure 5) and the depth of the crest of the western rift valley wall in the Rainbow region, taken from the *Smith and Sandwell* [1997] data set. The variability in depth and vertical structure of the θ_2/S offsets in individual profiles indicates that the interleaving cannot be viewed as a single coherent structure extending across the rift valley.

3. Rift Valley Hydrography and Flow Field

3.1. Stratification and Flow Observations

The shaded cells in Figure 6 show the horizontal distribution of potential density at 2200 m, i.e., at an intermediate depth between the peak of Rainbow Ridge (1950 m) and the saddle of Rainbow Sill (2500 m). The shading of each cell is determined by the pressure-averaged BRIDGET density measurements within its boundaries, with darker shades indicating higher densities. At 2200 m, SW basin water is generally denser than NE basin water. It is not clear if the high-density water is confined to the northeastern part of the SW basin because the lightly shaded cells found in the remainder of the basin are derived from few data points from single BRIDGET lines.

Figure 7 shows the pressure-averaged density and buoyancy frequency profiles of the two deep basins and Rainbow Sill (density only, calculated from a single along-sill tow-yo). The horizontal density difference between the basins has a maximum value of 4.5×10^{-3} near 2250 m. The different slopes of the density profiles between 2000 and 2250 m indicate that, on average, the isopycnals in this depth range are more spread in the NE basin than in the SW basin. This is confirmed by the corresponding buoyancy frequency profiles. While the stratification between 2300 and 2400 m is weaker in the NE basin than in the SW basin, there is no similar region in density space, i.e., the NE-basin stratification is weaker everywhere below $\sigma_2 = 36.922$ (2000 m). The stratification below 2400 m is too weak for the buoyancy frequencies to be resolved accurately.

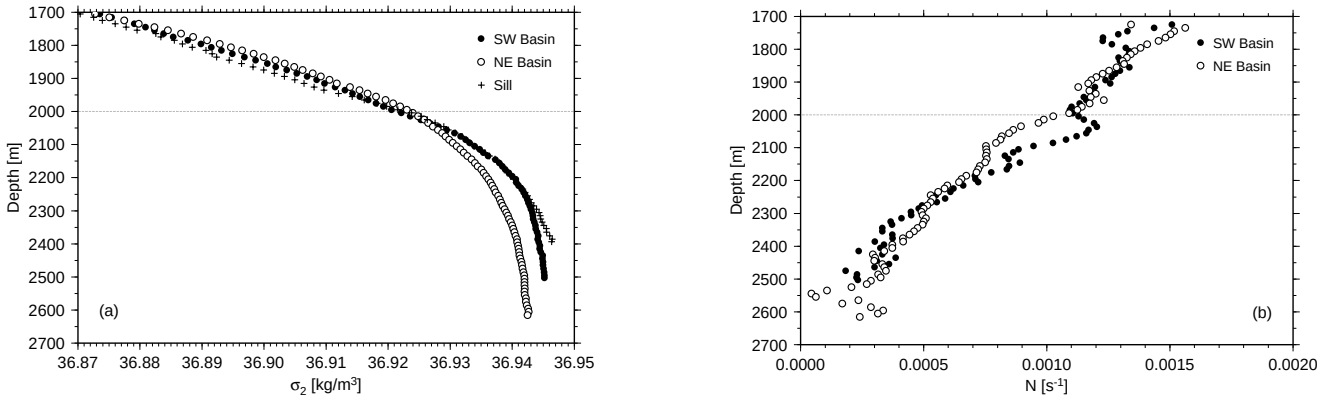

Figure 7. (a) Pressure-averaged density and (b) buoyancy frequency profiles of the SW basin, Rainbow Sill (density only) and the NE basin. Data points derived from <20 values for the basin profiles and from <5 values for the sill profile are not shown; the dotted lines at $2000\,\mathrm{m}$ indicate the depth below which the density profiles diverge.

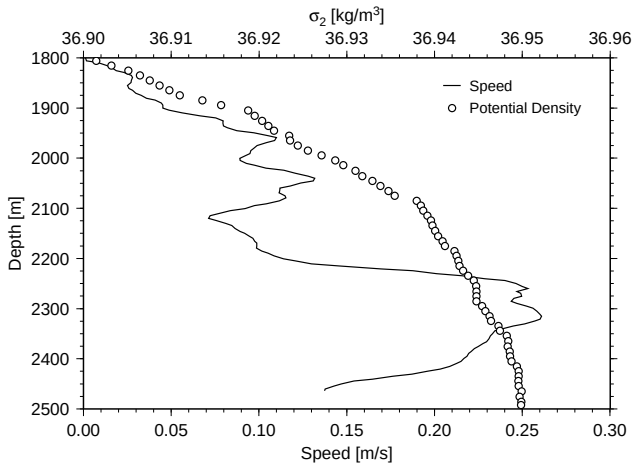

Figure 8. Flow speed and density profiles in the saddle of Rainbow Sill.

Inspection of the individual density profiles shows stable stratification extending to the bottom of the deepest profiles below $3200\,\mathrm{m}$, however. An estimate of $10^{-4}\,\mathrm{s}^{-1}$ is used in section 3.2 for the buoyancy frequency at $2500\,\mathrm{m}$.

In addition to the density distribution, Figure 6 also shows the LADCP current measurements at $2200\,\mathrm{m}$. The two main features to note are the consistent clockwise flow around the northern tip of Rainbow Ridge (the individual measurements were taken over a period of 3 weeks) and the strength of the currents on its western slope.

Figure 8 shows a flow speed profile from the saddle of Rainbow Sill. The vertical scale of the layer of strong flow peaking at $>0.25\,\mathrm{m\,s}^{-1}$ is $\approx 300\,\mathrm{m}$. Similar layers of intense currents are apparent in four out of the seven profiles from the western slope of Rainbow Ridge; they have vertical scales between 250 and $400\,\mathrm{m}$ and peak speeds between 0.17 and $0.28\,\mathrm{m\,s}^{-1}$. Figure 9 shows the vertical structure of the $50\,\mathrm{m}$-averaged current field derived from all seven stations on the slope. The layer of intense flow is confined to depths below $2000\,\mathrm{m}$ where its direction is much more uniform than above, indicating topographic steering.

Layers of intensified flow near the seabed were observed in profiles away from the western slope of Rainbow Ridge as well. They have typical vertical scales of $\approx 50\,\mathrm{m}$ and peak speeds between 0.1 and $0.15\,\mathrm{m\,s}^{-1}$. (It is interesting to note that a profile from the western slope of a different topographic high (at 33°45′W, 36°19′N) is similar to the ones from the western

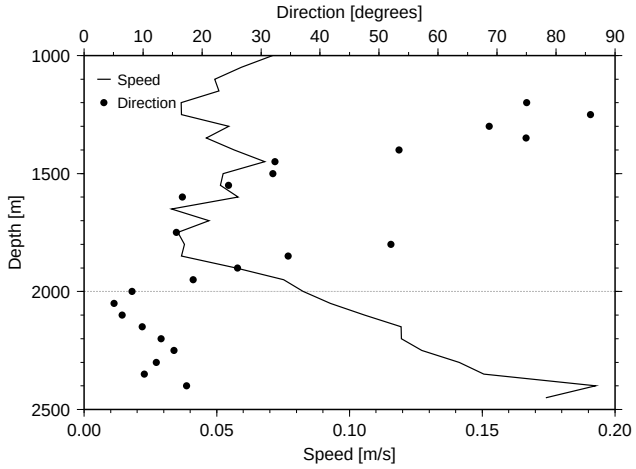

Figure 9. Pressure-averaged flow velocity on the western slope of Rainbow Ridge. Each data point represents a $50\,\mathrm{m}$ vertical mean; the dotted line is the same as in Figure 7.

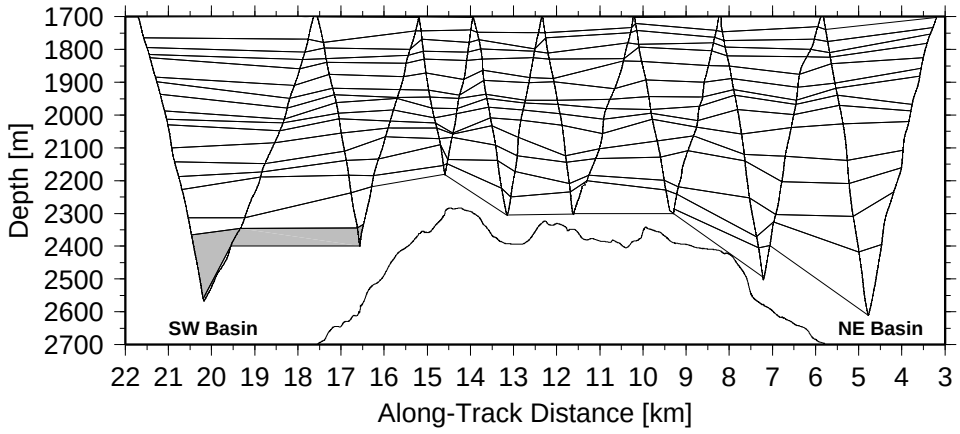

Figure 10. Isopycnal contours across Rainbow Sill. Contour levels were chosen for uniform spacing with depth; the shaded area indicates $\sigma_2 > 36.945$, found in the NE basin only below $2600\,\mathrm{m}$, except for a few profiles close to Rainbow Sill.

slope of Rainbow Ridge, with a vertical scale of $200\,\mathrm{m}$ and a peak speed of $0.19\,\mathrm{m\,s^{-1}}$.)

3.2. Flow Across Rainbow Sill

Figure 10 shows selected isopycnal contours from a tow-yo across Rainbow Sill (the black cross-sill tow of Figure 2). The contour levels were chosen so that their mean depths are uniformly spaced. The isopycnal surfaces of the densest water on the sill (near $14\,\mathrm{km}$) follow the topography descending into the NE basin, consistent with a northeastward overflow current. The associated vertical spreading of the isopycnals below $2000\,\mathrm{m}$ is indicative of mixing with NE-basin water. A second tow-yo across the sill, which was discarded because of instrument calibration problems (section 1.2), shows similar downsloping of the isopycnal surfaces in the NE basin below $2000\,\mathrm{m}$.

The densest water observed on Rainbow Sill (Figure 7) has a σ_2 value of 36.946, which corresponds to a potential temperature of $3.64°\mathrm{C}$, the same as the water found in the SW basin below $3000\,\mathrm{m}$ (section 2). This observation, together with the virtually identical θ_2/S characteristics in both basins (section 3.1), indicates that Rainbow Sill does not block the exchange

of water. The criterion for topographic blocking to occur in linearly stratified uniform flows across two-dimensional obstacles is that the dimensionless parameter $G = N' h_b / U' \gtrapprox 2$ for most obstacle shapes in nonrotating flows [*Baines*, 1987] and $G \gtrapprox 1.5$ for rotating flows over a Gaussian ridge [*Pierrehumbert and Wyman*, 1985], with N', U', and h_b denoting the upstream buoyancy frequency, velocity, and the height of the obstacle, respectively. Using $N' = 10^{-4}\,\mathrm{s}^{-1}$ (section 3.1), $U' = 0.05\,\mathrm{m\,s}^{-1}$ (typical LADCP velocity away from Rainbow Ridge), and $h_b = 700\,\mathrm{m}$ (height of Rainbow Sill above the SW-basin floor), G becomes 1.4, i.e., close to the limiting value. The uplifting of deep upstream water is driven by the dynamic pressure reduction caused by the large flow velocities across the sill, a phenomenon sometimes called Bernoulli aspiration [e.g., *Kinder and Bryden*, 1990].

The horizontal density gradient across Rainbow Sill is consistent with upstream influence of an obstacle, which has been observed for values of G as low as 0.75 [*Pierrehumbert and Wyman*, 1985]. The orientation of the corresponding pressure gradient implies a mean overflow from the SW into the NE basin. The observation that the density distributions of the individual tows are consistent with the mean picture suggests that the density-driven flow can be treated as quasi-steady. The mutual consistency of the LADCP measurements around Rainbow Ridge (Figure 6) and the lack of indications for flow reversal support this view and furthermore indicate that tidal effects (section 3.4) are weak compared to the density-driven flow. Additional evidence for quasi-steady along-valley flow is provided by the observation of a persistent northward current on the western flank of Rainbow Ridge throughout a 26-hour dive (with a remotely operated vehicle) in August 1996 [*German et al.*, 1996c] and by the along-valley density gradient observed in August–October 1992 [*Wilson et al.*, 1995], which is consistent with our data.

In the case of an inviscid steady two-dimensional flow along a channel of slowly varying geometry a horizontally asymmetric density distribution (i.e., differing reservoir conditions) implies that the flow is (hydraulically) controlled [*Armi*, 1986]. *Pratt* [1986] shows how the inviscid assumption of hydraulic models can be tested by evaluating the nondimensional parameter $P = C_d l / h$ (indicating the relative importance of hydraulic acceleration and deceleration caused by bottom friction), where $C_d (= 10^{-3})$, l, and h are the drag coefficient, the horizontal distance over which the thickness of the active lower layer (see below) changes significantly, and the mean thickness of that layer, respectively. Conservatively estimating $l = 15\,\mathrm{km}$ and $h = 300\,\mathrm{m}$ from Figure 10 results in an estimate of $P \approx 0.05$, indicating that frictional effects can be ignored. *Killworth* [1995] shows that the equivalence of hydraulic control and flow maximization known from nonrotating hydraulics holds for continuously stratified rotating flows controlled by sills and narrows of arbitrary topography as well. Therefore a hydraulic model can be used to estimate the volume flux across Rainbow Sill. The simple one-and-a-half layer reduced gravity model with zero upstream potential vorticity introduced by *Whitehead et al.* [1974] is considered adequate for this purpose, mainly because it is the simplest model of rotating hydraulics, which has been tested in similar contexts [*Whitehead*, 1997]. In the limit of no rotation it reduces to hydraulic flow over a weir.

Layer models require estimates for the density differences between the individual layers, which are assumed to be homogeneous. In real situations, separation of the water column into such layers is difficult except where there are sharp vertical temperature or salinity gradients coinciding with regions of high velocity shear. In the Rainbow profiles (e.g., Figure 8), there are no clear indications for such layers. *Whitehead* [1989] proposes a simple method for dealing with this problem, based on the observation that in hydraulically controlled stratified flows there is generally a well-defined bifurcation depth below which the data can be separated into high-density (upstream) and low-density (downstream) profiles. The bifurcation depth is taken to be the upstream depth of the interface between the two model layers, which makes this method equivalent to defining the interface as the maximum density surface that remains horizontal over the sill [e.g., *Mercier and Bryden*, 1994]. The density difference between the active lower and the passive upper layers is set to the maximum horizontal upstream-downstream difference between the bifurcation depth and the sill depth. (This method yields correct values for homogeneous layers.) The respective values for the flow across Rainbow Sill are $2000\,\mathrm{m}$ for the bifurcation depth and 4.5×10^{-3} for the density difference (Figure 7), resulting in a reduced gravity estimate of $g' \approx 4.5 \times 10^{-5}\,\mathrm{m\,s}^{-2}$. The vertical scale $h_u = 500\,\mathrm{m}$ of the flow between the bifurcation depth and the sill depth is consistent with the intensified current layer shown in Figure 9.

The model of *Whitehead et al.* [1974] is now applied to estimate the volume flux Q and the width w of the overflow current. The respective expressions for a sill which is wide compared to the internal Rossby radius of deformation are $Q = g' h_u^2 / (2f)$ and $w = (2g' h_u)^{1/2} / f$. As suggested by *Whitehead* [1989], we use the sill width at the bifurcation depth for the comparison; its value of $7.5\,\mathrm{km}$, taken from bathymetric charts, is much larger than the corresponding Rossby radius $(g' h_u)^{1/2} / f \approx 1.7\,\mathrm{km}$, where $f = 8.6 \times 10^{-5}\,\mathrm{s}^{-1}$ is the Coriolis parameter at 36°N. The volume flux and current-width estimates become $Q \approx 65 \times 10^3\,\mathrm{m}^3\,\mathrm{s}^{-1}$ and $w \approx 2.5\,\mathrm{km}$, respectively. The Rossby number of the flow $\mathrm{Ro} = U / fl \approx 0.5$ (based on the half width of Rainbow Sill ($l_s \approx 5\,\mathrm{km}$) and the velocity scale of $0.2\,\mathrm{m\,s}^{-1}$, estimated from Figure 9) indicates

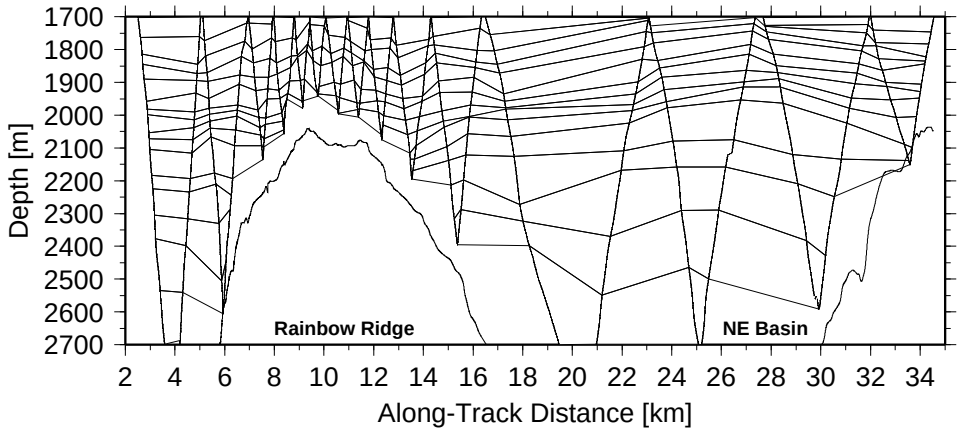

Figure 11. Isopycnal contours across Rainbow Ridge. Contour levels are the same as in Figure 10.

that the model assumption of geostrophically adjusted flow across the sill is at least partially violated. Effects of steady or time-variable (e.g., tidal) barotropic forcing are ignored.

3.3. Topographic Wake

The mean density stratification of the two deep basins (Figure 7) suggests that the hydraulically controlled flow is confined to depths below $2000\,\mathrm{m}$. Between the bifurcation depth and the peak of Rainbow Ridge at $1950\,\mathrm{m}$ the incident current, of order $0.05\,\mathrm{m\,s^{-1}}$ (Figure 9), flows over and around the topography. Evaluating G (section 3.2) with $N' = 10^{-3}\,\mathrm{s^{-1}}$ (Figure 7b) and $h_b = 50\,\mathrm{m}$ yields a value of 1.0, indicating that blocking is unlikely. The characteristic half width l_p of the top $50\,\mathrm{m}$ of Rainbow Ridge is 1–2 km. Because $l_p \gg U'/N' = 50\,\mathrm{m}$, nonhydrostatic effects may be ignored, while the corresponding Rossby number of 0.3–0.6 indicates that rotational effects are important.

The appropriate flow regime for these parameters is the rotating wave regime of *Queney* [1948; see also *Gill,* 1982]. The corresponding lee waves radiate energy (group velocity) upward and downcurrent at an angle between 1° and 90° to the horizontal. The horizontal wavelength λ of the pattern of vertical streamline displacement close to a bell-shaped ridge is $2\pi U'/f$, which is $\approx 4\,\mathrm{km}$ using the Rainbow parameters. Because λ is comparable to the width of the peak of Rainbow Ridge, large-amplitude lee waves are expected. Figure 11 shows a selection of isopycnal contours from a BRIDGET line across Rainbow Ridge (the black cross-ridge tow of Figure 2). The pattern of isopycnal surface displacement found in the lee of the ridge is consistent with the rotating wave regime because it is confined to the quadrant upward and downstream of the ridge peak and the wavelength directly over the peak is $\approx 5\,\mathrm{km}$. (The doming of the isopycnals in the eastern part of the NE basin is not considered to be a topographic effect but is consistent with tidal motion; see section 3.4.) Two additional BRIDGET tows across Rainbow Ridge show similar wave-like features, although the patterns there are less clear because of the decreased horizontal resolution caused by larger towing velocities. These additional observations together with the horizontal extent of the lee wave patterns ($\approx 10\,\mathrm{km}$) indicate that the topographic wake is most likely set up by the mean flow (a velocity of order $0.5\,\mathrm{m\,s^{-1}}$ would be required to propagate a disturbance over a distance of $10\,\mathrm{km}$ in half a tidal period).

3.4. Hydrographic Variability on Tidal Timescales

One of the main problems regarding the interpretation of hydrographic surveys like the one presented here is the difficulty in separating spatial and temporal scales, especially in the tidal range. (On the basis of resampling of the same region over the 4-week data collection period, a measurable shift of the hydrography over timescales of the order of weeks can be excluded.) To investigate the variability of the hydrography on tidal timescales, a 10-hour CTD yo-yo was done at a station close to Rainbow Sill (the solid star with a white border of Figure 2). Unfortunately, the LADCP failed during the cast. Figure 12 shows the evolution of the isopycnal surfaces during sampling. Between the upper turning point of 1600 and $\approx 2250\,\mathrm{m}$ they exhibit a wave-like structure consistent with the semidiurnal tidal period. The phase of the isopycnal displacement appears

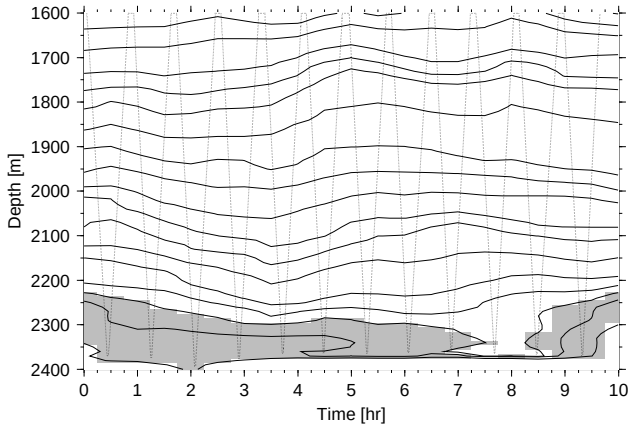

Figure 12. Isopycnal contours of the 10-hour CTD yo-yo. Contour levels and shading are the same as in Figure 10.

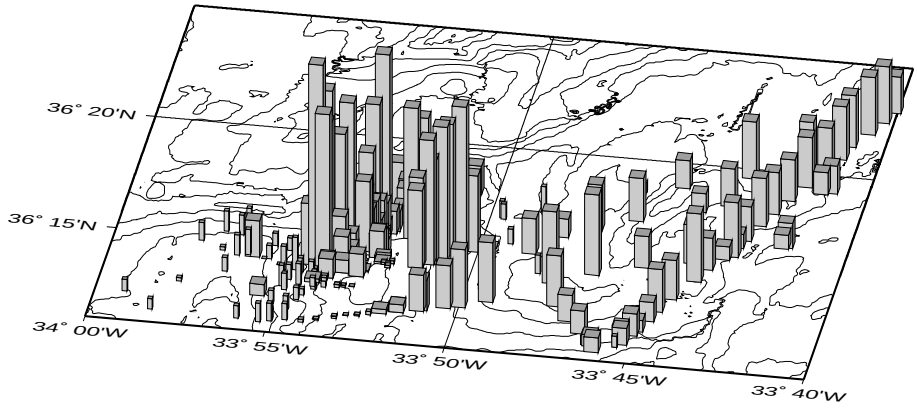

Figure 13. Depth-integrated (1500–2500 m) nephelometry profiles of the BRIDGET data set (arbitrary vertical scale). Bathymetric contours are the same as in Figure 1; thin bars denote profiles without plume signals (from visual inspection).

to vary with depth. The maximum amplitude near 1800 m is >100 m, but displacements of order 50 m are more typical. Close to the seafloor the structure is more complex; the potential-density inversions at 4.5, 7, and 8.5 hours are not contouring artifacts. (There are indications from the CTD altimeter for some horizontal instrument displacement during the cast.)

The pattern of the isopycnals shown in Figure 11 is therefore most likely caused by a combination of spatial and temporal variability during the 12-hour sampling time. If the doming of the isopycnals in the NE basin were a spatial feature, it would imply anticyclonic flow around the basin, which is inconsistent both with direct velocity measurements (e.g., Figure 6) and with density observations from four additional tows crossing the same basin in different directions.

4. Hydrothermal Particle Plume

Figure 13 shows the horizontal distribution of the depth-integrated BRIDGET nephelometry profiles. (The entire data set was used, including the tows with the faulty CTD instrument; see section 1.2). In the SW basin the plume signals are confined to the area north of the vent field, consistent with the density and flow observations of section 3. Upstream of Rainbow Sill the horizontal variability between neighboring profiles is highest, whereas downstream, on the eastern slope of Rainbow Ridge, the depth-integrated plume signals are more uniform. The drop-off in signal strength away from the ridge (east of

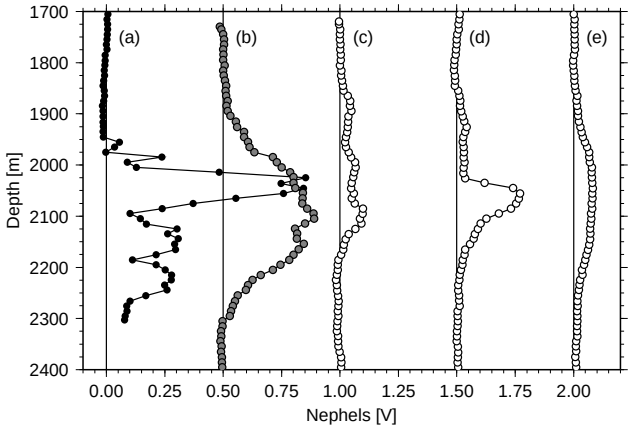

Figure 14. Selected BRIDGET nephelometry profiles, including (a) the one closest ($<200\,\mathrm{m}$) to the vent field, (b) one from the eastern slope of Rainbow Ridge, (c and d) two adjacent ones from a single tow-yo near the center of the NE basin, and (e) the one farthest away ($\approx 30\,\mathrm{km}$) from the vent field. Successive profiles are horizontally offset by $0.5\,\mathrm{V}$.

33°50′W) is consistent with horizontal mixing and coincides with the boundary between the ridge slope, where hydrographic interleaving is observed, and the basin interior, where no interleaving is apparent (section 2). Particle settling and dissolution provide alternative mechanisms for the decrease in plume nephels; the small flow velocities in the NE basin (e.g., Figure 6) are consistent with increased sedimentation rates. Within the NE basin the integrated plume signals decrease south of ≈36°15′N, suggesting that the plume does not follow the isobaths around the basin, consistent with the nephelometry section shown in Figure 3 of *German et al.* [1998] (BRIDGET tow 04, the density section of which is shown in our Figure 11) as well as with the methane distribution presented there.

A plot of the horizontal distribution of the nephelometry maxima is similar to Figure 13, the main difference being a reduction in signal strength of ≈30% across Rainbow Sill (see also Figure 15), consistent with vertical mixing.

On the basis of the horizontal distribution of the nephelometry anomalies, the BRIDGET plume data (thick bars in Figure 13) were separated into three regions: SW basin, eastern slope of Rainbow Ridge, and NE basin interior (east of 33°50′W). Figure 14 shows nephelometry profiles from each of these regions, selected to illustrate the variability throughout the domain of observation.

In the near-source profiles (upstream of Rainbow Sill) the nephelometry anomalies are confined between $2300\,\mathrm{m}$ (the depth of the vent field) and $1900\,\mathrm{m}$. They are characterized by one to four peaks, with the signal between peaks often dropping to background values. Similar vertically structured particle distributions are commonly observed close to hydrothermal sources [e.g., *Rosenberg et al.,* 1988; *Rudnicki and Elderfield,* 1992]. In the FLAME data, individual nephelometry peaks cannot be traced between profiles, suggesting that the horizontal scale of the coherent plume fluid structures is small (typical BRIDGET tow-yo spacing at plume depth is 1–2 km).

For each of the three regions a mean profile derived from the BRIDGET plume data set is shown in Figure 15. Because of the tidal variability of the hydrography, which has a vertical scale comparable to the thickness of individual near-source nephelometry peaks (section 3.4), averaging of both nephels and depth was performed in potential-density space with variable bin sizes depending on the stratification. All three mean profiles are approximately Gaussian in depth, without indications for vertical structure. (The CTD data set is not extensive enough to derive similar mean profiles.) The Gaussian curve fitted to the SW-basin profile is centered at $\mu = 2120\,\mathrm{m}$, with a thickness (1 standard deviation) of $\sigma = 96\,\mathrm{m}$, a peak value of $\Delta n^* = 0.25\,\mathrm{V}$, and an RMS error of $0.018\,\mathrm{V}$; the respective values for the profile from the eastern slope of Rainbow Ridge are $\mu = 2120\,\mathrm{m}$, $\sigma = 102\,\mathrm{m}$, $\Delta n^* = 0.18\,\mathrm{V}$, and RMS error $0.009\,\mathrm{V}$; and those for the NE-basin interior profile are $\mu = 2100\,\mathrm{m}$, $\sigma = 137\,\mathrm{m}$, $\Delta n^* = 0.06\,\mathrm{V}$, and RMS error $0.004\,\mathrm{V}$, respectively. The peak of the mean plume exhibits no vertical trend with distance from the source (neither in depth nor in density space), indicating that the profiles of Figure 15 represent the equilibrium plume. The lack of evidence for vertical overshoot (plume cap) near the source is consistent with laboratory [e.g., *Helfrich and Battisti,* 1991] and numerical [e.g., *Lavelle,* 1997] experiments, which show that both rotation

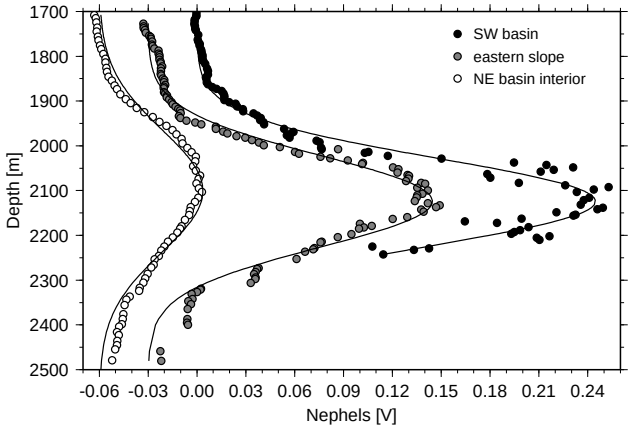

Figure 15. Density-averaged BRIDGET nephelometry profiles and depth-fitted Gaussian curves of the SW basin (solid circles), the eastern slope of Rainbow Ridge (shaded circles, offset by $-0.03\,\mathrm{V}$), and the interior of the NE basin (open circles, offset by $-0.06\,\mathrm{V}$). The SW/slope/NE profiles are derived from 26/17/68 casts, respectively; mean values calculated from <4 data points are not shown.

and cross flows tend to suppress such an overshoot. The height of rise measured at the mean nephelometry maximum is $200\,\mathrm{m}$.

5. Heat Flux Estimates

One simple method for estimating heat fluxes from hydrothermal plumes is based on source buoyancy flux estimates derived from height-of-rise observations and more or less elaborate models of the buoyant plumes [e.g., *Rudnicki and Elderfield*, 1992]. Even the most advanced current models cannot resolve plumes from individual sources within a vent field and must rely on the assumption of a single point or line source (i.e., the length scale associated with the extent of the source is assumed to be much smaller than the plume rise height) [*Lavelle*, 1997]. If this assumption is violated, the buoyancy flux estimated from the rise height of the model plume can significantly underestimate the true buoyancy flux because the effects of plume interaction at some height above the sources are ignored. Applying a simple plume model to the observed near-source hydrography and rise height (similar to *Rudnicki and Elderfield* [1992]) yields a heat flux estimate of $0.3\,\mathrm{GW}$ [*Thurnherr*, 2000]. The individual vent chimneys at Rainbow are distributed over an area of $100\,\mathrm{m}\times250\,\mathrm{m}$ [*Fouquet et al.*, 1998], so that the extent of the integrated plume source is of the same order as the observed rise height. Because the point source assumption is violated, this heat flux estimate is not considered accurate.

To derive a better estimate, we use an alternative approach based on the advective flux of the temperature anomalies associated with the equilibrium plume [*Baker and Massoth*, 1987]. The Gaussian shape of the mean plume (Figure 15) supports the assumption of quasi-steadiness, so that the equilibrium temperature anomaly flux can be defined as

$$Q_e\overline{\Delta\theta_e} = \int \Delta\theta_e u_n dE, \tag{1}$$

where Q_e is the volume flux carrying the spatially averaged equilibrium temperature anomaly $\overline{\Delta\theta_e}$ away from the "source" (which in this context is the region where the buoyant plumes become neutrally buoyant). The integral is evaluated over a suitably defined surface E across which the entire equilibrium plume is advected with velocity u_n (normal to E), away from the source.

If the T/S relationship of the background fluid entrained into the buoyant plumes is linear, the equilibrium temperature anomaly flux $Q_e\overline{\Delta\theta_e}$ is related to the corresponding source temperature anomaly flux $Q_i\overline{\Delta\theta_i}$ [from *McDougall*, 1990,

expression (22)] by

$$\frac{Q_i\overline{\Delta\theta_i}}{Q_e\overline{\Delta\theta_e}} = \frac{1-R_\rho}{1-R_\rho/R_\rho^i}, \tag{2}$$

where $R_\rho = (\alpha\theta_z)/(\beta S_z)$ is the stability ratio of the water column (with α and β denoting the linear thermal expansion and haline contraction coefficients, respectively, evaluated at the reference pressure of potential temperature) and $R_\rho^i = (\alpha\overline{\Delta\theta_i})/(\beta\overline{\Delta S_i})$ is the density anomaly ratio of the hydrothermal source fluid (with $\overline{\Delta S_i}$ denoting its mean salinity anomaly). Even though *McDougall* [1990] assumes the vertical gradients of background potential temperature and salinity to be constant, this assumption is not used in his derivation of expression (22); it is sufficient to assume that R_ρ is constant, i.e., that the background T/S is linear. (*Lavelle et al.* [1998] arrive at the same conclusion using a different derivation.) The stability ratio $R_\rho = 2.36\ (\pm 0.11)$ is taken from the near-source CTD profiles in the depth range of plume rise (1900–2300 m), with $\alpha = 1.47 \times 10^{-4}\ ^\circ\mathrm{C}^{-1}$ and $\beta = 7.53 \times 10^{-4}\ \mathrm{psu}^{-1}$ at 4°C and 2000 dbar [*Gill*, 1982]. The same coefficients are used to estimate the source fluid density anomaly ratio $R_\rho^i \approx 5.4$ from the Rainbow effluent properties [*Fouquet et al.*, 1998]. The source heat flux H is calculated using

$$H = \rho_i c_p Q_i \overline{\Delta\theta_i}, \tag{3}$$

where $\rho_i \approx 993\,\mathrm{kg\,m^{-3}}$ is the density calculated from the effluent properties with the linear equation of state expanded at the background temperature and salinity, and $c_p \approx 4.2 \times 10^3\,\mathrm{J\,kg^{-1}\,K^{-1}}$ is the specific heat of the ambient sea water [*Turner and Campbell*, 1987].

The isopycnal temperature anomalies associated with the Rainbow light-scattering plume are estimated using a new method derived by *Thurnherr* [2000]. On the basis of the assumption of linear background θ_2/S (or, equivalently, linear background θ_2/σ_2) properties within the particle plume the nephelometry anomalies Δn of the near-source CTD profiles were found to be linearly correlated with the corresponding temperature anomalies, allowing the temperature profile within each particle peak to be written as

$$\theta_2(z) = A + B\sigma_2(z) + C\Delta n(z). \tag{4}$$

Expression (4) can be fitted to each nephelometry peak, resulting in independent estimates for the regression coefficients A, B, and C from which the isopycnal temperature anomalies are calculated using

$$\Delta\theta_2(z) = \theta_2(z) - (A + B\sigma_2(z)). \tag{5}$$

The mean (± 1 standard deviation) estimate of the temperature versus nephelometry anomaly slope C of the BRIDGET data set is $-0.019\ (\pm 0.005)^\circ\mathrm{C\,V^{-1}}$, similar to the value of $-0.019\ (\pm 0.003)^\circ\mathrm{C\,V^{-1}}$ derived from the CTD profiles [*Thurnherr*, 2000]. These results are consistent with the observation that the nephelometers used on the two platforms had similar response characteristics (section 1.2). The mutual consistency of the individual slope estimates implies that the near-source Gaussian plume shown in Figure 15 can be rescaled to yield the mean temperature anomaly profile $\Delta\theta_e(z)$; its peak value is $-4.8 \times 10^{-3}\ ^\circ\mathrm{C}$.

The heat flux is now estimated using expressions (1)–(3). We assume the plume to be laterally uniform across its entire (cross-valley) width of 2 km [*German et al.*, 1998] and the mean near-source current profile between 1900 and 2300 m to be approximated by

$$u_n(z) = u_0 + \frac{\partial u}{\partial z}(z - z_0), \tag{6}$$

with $u_0 = 0.05\,\mathrm{m\,s^{-1}}$, $\partial u/\partial z = 2.5 \times 10^{-4}\,\mathrm{s^{-1}}$, and $z_0 = 1900\,\mathrm{m}$ (Figure 9). Integrating $\Delta\theta_e(z)u_n(z)$ between 1900 and 2300 m and across the plume width yields $Q_e\overline{\Delta\theta_e} \approx -230^\circ\mathrm{C\,m^3\,s^{-1}}$. Using expression (2), the source temperature anomaly flux becomes $Q_i\overline{\Delta\theta_i} \approx 550^\circ\mathrm{C\,m^3\,s^{-1}}$, resulting in a heat flux estimate of 2.3 GW. Considering the number of assumptions and estimates this value is based on, it is difficult to determine a confidence interval. In contrast to the rise height method none of the parameters is raised to a power greater than 1, however, and those with the greatest uncertainties, namely the width of the plume and the mean current velocity, are most likely good to at least within a factor of 2. Our estimates for the lower and upper bounds of the heat flux are 1 GW and 5 GW, respectively.

6. Discussion

Measurements of the hydrography and flow field during the FLAME cruise as well as plume dispersal observations suggest a mean circulation in the Rainbow region as shown schematically in Figure 16. The flow below 2000 m forms a strong

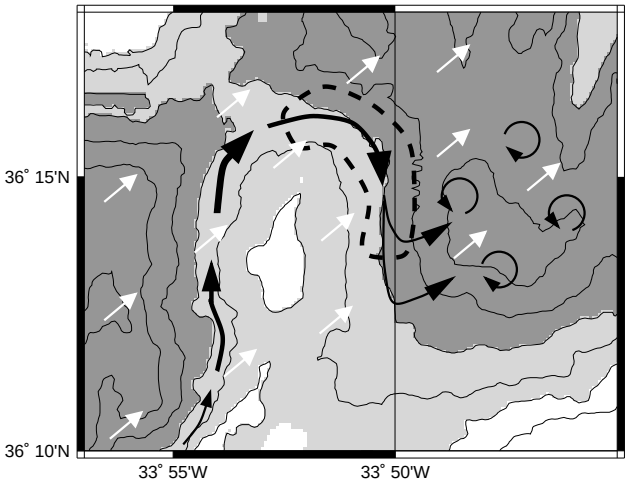

Figure 16. Sketch of the mean flow regime around Rainbow Ridge. Topographic shading and contours are the same as in Figure 1; solid arrows represent the hydraulically controlled flow below 2000 m; dashed line indicates the region where enhanced mixing is expected; open arrows represent the flow above 2000 m.

northward boundary current along the western slope of Rainbow Ridge and across Rainbow Sill, which acts as a hydraulic control point. Downstream of the sill the overflow current descends into the NE basin while continuing to flow clockwise around Rainbow Ridge. The downslope current mixes with NE-basin water and gradually decreases in strength. Eventually, it detaches from the eastern slope of the ridge, carrying particle-rich plume fluid into the interior of the basin. Above 2000 m, the mean flow over the peak of Rainbow Ridge generates lee waves which radiate energy upward and downstream.

At plume height the flow is controlled by a combination of rotation, stratification, and topographic effects, while an influence of the hydrothermal plume on the dynamics is not observed. Dispersal of the hydrothermal material is dominated by the hydraulically controlled overflow, which carries the bulk of the equilibrium plume northeastward along the rift valley. A small fraction of the particle plume extends above the minimum depth of the blocking topography, indicating that some hydrothermal material may be advected across the peak of Rainbow Ridge.

Upstream of Rainbow Sill, close to the vent field, the horizontal and vertical variability of the nephelometry profiles is highest, similar to observations from other hydrothermal sites. The mutually consistent linear correlations between nephels and hydrographic anomalies in the near-source profiles [*Thurnherr,* 2000] indicate that this variability is not caused by nonconservative particle behavior but represents varying plume fluid concentrations. The Gaussian shape of the density-averaged near-source particle plume implies that the peaks of the individual profiles do not represent layers in the sense of *Rudnicki and Elderfield* [1992].

The vertical scale of the near-source nephelometry peaks is of the order of 100 m, while failure to trace individual peaks between consecutive BRIDGET tow-yo casts yields an upper bound of 1–2 km for the corresponding horizontal scale. It is not clear whether these scales are controlled by processes associated with steady convection or with source or background variability. Laboratory [e.g., *Papantoniou and List,* 1989] and numerical experiments [e.g., *Lavelle,* 1997] show that plumes rising from single steady buoyancy sources into quiescent or uniformly flowing backgrounds result in highly inhomogeneous plume fluid concentrations. Assuming that the scales of the coherent structures in the Rainbow equilibrium plume are determined by a balance between rotation and stratification effects (i.e., assuming a Burger number Nh/fl of order 1, where l and h are horizontal and vertical length scales, respectively [e.g., *Helfrich and Battisti,* 1991]), yields a horizontal/vertical aspect ratio of 10 at the mean plume depth, consistent with the observations.

The Gaussian shape of the density-averaged nephelometry profiles, to our knowledge the first such observation in a hydrothermal context, indicates that the steady state plume was adequately sampled during the FLAME cruise. The mean plume occupies the entire depth range between the vent field and the maximum rise height, indicating that the height of rise cannot

adequately be estimated from individual profiles. On the basis of the linear relationship between the near-source nephelometry and the corresponding temperature anomalies, and the mean flow near the vent field, the temperature anomaly flux of the equilibrium plume was used to derive a heat flux estimate of $2.3\,\mathrm{GW}$ associated with the particle plume.

A second heat flux estimate, based on height-of-rise modeling, is an order of magnitude smaller. *Fouquet et al.* [1998, p. 26] describe the distribution of the vent chimneys at Rainbow as "about ten major groups of extremely active black smokers." The two heat flux estimates are mutually consistent if the plumes from the different vent groups coalesce high enough in the water column so that they have already lost much of their buoyancy, i.e., if the rise height is determined by the buoyancy flux of a single group of vents, for which the point source assumption is valid. (On the basis of Figure 1 of *Fouquet et al.* [1998] the distance between neighboring vent groups ranges between $\approx$25 and $75\,\mathrm{m}$.)

Combining hydrographic, flow field, and particle plume observations has yielded a number of novel insights into the dynamical processes acting within the rift valley of the Mid-Atlantic Ridge, where they control the dispersal of a hydrothermal plume. The analysis of the regional circulation will aid in the interpretation of biological and geochemical data because it constrains the pathways and ages of the measurements. The mean near-source nephelometry and temperature anomaly profiles can be rescaled in terms of other conservative hydrothermal tracers or, using expression (2), to yield a mean dilution profile. This will allow the corresponding fluxes to be calculated in the same way we derived our heat flux estimate.

Acknowledgments. We would like to thank the BRIDGET team Chris German, Bob Kirk, Mark Rudnicki, and Steve Riches for support at sea and acquisition of the FLAME data set, Mai Mai Lam for processing the LADCP data, and the officers and crew of RRS *Discovery.* The encouragement and constructive criticism of the two reviewers, Kevin Speer and an anonymous reviewer, are gratefully acknowledged. This work was funded by ECMAST(III) project "AMORES" (contract MAST3-CT95-0040). The FLAME cruise (RRS Discovery 228) was funded by the BRIDGE Grant 85 (Fluxes at AMAR Experiment). Additional support for one of the authors (A.M.T.) was provided by a studentship of the University of Southampton and UNESCO.

References

Armi, L., The hydraulics of two flowing layers with different densities, *J. Fluid. Mech., 163,* 27–58, 1986.

Baines, P. G., Upstream blocking and airflow over mountains, *Annu. Rev. Fluid Mech., 19,* 75–97, 1987.

Baker, E. T., G. J. Massoth, Characteristics of hydrothermal plumes from two vent fields on the Juan de Fuca Ridge, northeast Pacific Ocean, *Earth Planet. Sci. Lett., 85,* 59–73, 1987.

Elderfield, H., A. Schultz, Mid-ocean ridge hydrothermal fluxes and the chemical composition of the ocean, *Annu. Rev. Earth Planet. Sci., 24,* 191–224, 1996.

Fouquet, Y., et al., FLORES diving cruise with the Nautile near the Azores — First dives on the Rainbow field: Hydrothermal seawater/mantle interaction, *InterRidge News, 7,* 24–28, 1998.

German, C. R., G. P. Klinkhammer, M. D. Rudnicki, The Rainbow hydrothermal plume, $36°15'$N, Mid-Atlantic Ridge, *Geophys. Res. Lett., 23,* 2979–2982, 1996a.

German, C. R., L. M. Parson, the HEAT Scientific Team, Hydrothermal exploration at the Azores triple-junction: Tectonic control of venting at slow-spreading ridges?, *Earth Planet. Sci. Lett., 138,* 93–104, 1996b.

German, C. R., L. M. Parson, C. Wilson, G. P. Klinkhammer, D. J. Fornari, S. E. Humphris, The geologic setting of the Rainbow hydrothermal field, Mid-Atlantic Ridge (abstract), *Eos Trans. AGU, 77(46),* Fall Meet. Suppl., F707, 1996c.

German, C. R., K. J. Richards, M. D. Rudnicki, M. M. Lam, J. L. Charlou, the FLAME Scientific Party, Topographic control of a dispersing hydrothermal plume, *Earth Planet. Sci. Lett., 156,* 267–273, 1998.

Gill, A. E., *Atmosphere-Ocean Dynamics,* 662 pp., Academic, San Diego, Calif., 1982.

Ginster, U., M. J. Mottl, R. P. Von Herzen, Heat flux from black smokers on the Endeavor and Cleft segments, Juan de Fuca Ridge, *J. Geophys. Res., 99,* 4937–4950, 1994.

Gould, W. J., Physical oceanography of the Azores front, *Prog. Oceanogr., 14,* 167–190, 1985.

Helfrich, K. R., T. Battisti, Experiments on baroclinic vortex shedding from hydrothermal plumes, *J. Geophys. Res., 96,* 12,511–12,518, 1991.

Killworth, P. D., Hydraulic control and maximal flow in rotating stratified hydraulics, *Deep Sea Res., Part I, 42,* 859–871, 1995.

Kinder, T. H., H. L. Bryden, Aspiration of deep waters through straits, in *The Physical Oceanography of Sea Straits*, edited by L. J. Pratt, pp. 295–319, Kluwer Acad., Norwell, Mass., 1990.

Lavelle, J. W., Buoyancy-driven plumes in rotating, stratified cross flows: Plume dependence on rotation, turbulent mixing, and cross-flow strength, *J. Geophys. Res., 102,* 3405–3420, 1997.

Lavelle, J. W., E. T. Baker, G. J. Massoth, On the calculation of total heat, salt and tracer fluxes from ocean hydrothermal events, *Deep Sea Res., Part II, 45,* 2619–2636, 1998.

McDougall, T. J., Bulk properties of "hot smoker" plumes, *Earth Planet. Sci. Lett., 99,* 185–194, 1990.

Mercier, H., H. L. Bryden, Flow of antarctic bottom water over the sill in the Romanche fracture zone, *Int. WOCE Newsl., 17,* 9–10, 1994.

Papantoniou, D., E. J. List, Large-scale structure in the far field of buoyant jets, *J. Fluid. Mech., 209,* 151–190, 1989.

Pierrehumbert, R. T., B. Wyman, Upstream effects of mesoscale mountains, *J. Atmos. Sci., 42,* 977–1003, 1985.

Pratt, L. J., Hydraulic control of sill flow with bottom friction, *J. Phys. Oceanogr., 16,* 1970–1980, 1986.

Queney, P., The problem of air flow over mountains: A summary of theoretical studies, *Bull. Am. Meteorol. Soc., 29,* 16–26, 1948.

Rosenberg, N. D., J. E. Lupton, D. Kadko, R. Collier, M. D. Lilley, H. Pak, Estimation of heat and chemical fluxes from a seafloor hydrothermal vent field using Radon measurements, *Nature, 334,* 604–607, 1988.

Rudnicki, M. D., H. Elderfield, Theory applied to the Mid-Atlantic Ridge hydrothermal plumes: The finite-difference approach, *J. Volcanol. Geotherm. Res., 50,* 161–172, 1992.

Rudnicki, M. D., C. R. German, R. E. Kirk, M. Sinha, H. Elderfield, S. Riches, New instrument platform tested at Mid-Atlantic Ridge, *Eos Trans. AGU, 76,* 329–330, 1995.

Saunders, P. M., T. J. Francis, The search for hydrothermal sources on the Mid-Atlantic Ridge, *Prog. Oceanogr., 14,* 527–536, 1985.

Schultz, A., H. Elderfield, Controls on the physics and chemistry of seafloor hydrothermal circulation, *Philos. Trans. R. Soc. London, Ser. A, 355,* 387–425, 1997.

Smith, W. H., D. T. Sandwell, Bathymetric prediction from dense altimetry and sparse shipboard bathymetry, *J. Geophys. Res., 99*, 21,803–21,824, 1997.

Sy, A., Investigation of large-scale circulation patterns in the central North Atlantic: The North Atlantic Current, the Azores Current, and the Mediterranean Water plume in the area of the Mid-Atlantic Ridge, *Deep Sea Res., Part A, 35*, 383–413, 1988.

Thurnherr, A. M. Hydrography and flow in the rift valley of the Mid-Atlantic Ridge, Ph. D. thesis, School of Ocean and Earth Science, Univ. of Southampton, England, 2000.

Tunnicliffe, V., The biology of hydrothermal vents: Ecology and evolution, in *Oceanography and Marine Biology, An Annual Review*, vol. 29, edited by M. Barnes, pp. 319–407, Aberdeen Univ. Press, Scotland, 1991.

Turner, J. S., I. H. Campbell, Temperature, density and buoyancy fluxes in "black smoker" plumes, and the criterion for buoyancy reversal, *Earth Planet. Sci. Lett., 86*, 85–92, 1987.

Whitehead, J. A., Internal hydraulic control in rotating fluids — applications to oceans, *Geophys. Astrophys. Fluid Dyn., 48*, 169–192, 1989.

Whitehead, J. A., Critical control at deep ocean passages, *Int. WOCE Newsl., 28*, 14–17, 1997.

Whitehead, J. A., A. Leetmaa, R. A. Knox, Rotating hydraulics of straits and sill flows, *Geophys. Fluid Dyn., 6*, 101–125, 1974.

Wilson, C., K. Speer, J.-L. Charlou, H. Bougault, G. Klinkhammer, Hydrography above the Mid-Atlantic Ridge (33°–40°N) and within the Lucky Strike segment, *J. Geophys. Res., 100*, 20,555–20,564, 1995.

K. J. Richards, School of Ocean and Earth Science, Southampton Oceanography Centre, Southampton SO14 3ZH, England, UK. (K.J.Richards@soc.soton.ac.uk)

A. M. Thurnherr, Dept. of Oceanography, Florida State University, Tallahassee, FL 32306-4320. (A.Thurnherr@ocean.fsu.edu)

Received July 28, 1998; revised December 1, 1999; accepted January 31, 2000.